

Article

Halide-Doping Effect of Strontium Cobalt Oxide Electrocatalyst and the Induced Activity for Oxygen Evolution in an Alkaline Solution

Mohamed A. Ghanem ^{1,*}, Mabrook S. Amer ^{1,2}, Abdullah M. Al-Mayouf ^{1,2}, Prabhakarn Arunachalam ¹ and Mark T. Weller ³

¹ Chemistry Department, College of Science, King Saud University, Riyadh 11451, Saudi Arabia; msamer@ksu.edu.sa (M.S.A.); amayouf@ksu.edu.sa (A.M.A.-M.); parunachalam@ksu.edu.sa (P.A.)

² K.A.CAR Energy Research and Innovation Center at Riyadh, King Saud University, Riyadh 11451, Saudi Arabia

³ Chemistry Department, Cardiff University, Cardiff CF10 3AT, UK; wellerm1@cardiff.ac.uk

* Correspondence: mghanem@ksu.edu.sa; Tel.: +966-011-4670405

Abstract: Perovskites of strontium cobalt oxyhalides having the chemical formulae $\text{Sr}_2\text{CoO}_{4-x}\text{H}_x$ (H = F, Cl, and Br; x = 0 and 1) were prepared using a solid-phase synthesis approach and comparatively evaluated as electrocatalysts for oxygen evolution in an alkaline solution. The perovskite electrocatalyst crystal phase, surface morphology, and composition were examined by X-ray diffraction, a scanning electron microscope, and energy-dispersive X-ray (EDX) mapping. The electrochemical investigations of the oxyhalides catalysts showed that the doping of F, Cl, or Br into the Sr_2CoO_4 parent oxide enhances the electrocatalytic activity for the oxygen evolution reaction (OER) with the onset potential as well as the potential required to achieve a current density of 10 mA/cm^2 shifting to lower potential values in the order of Sr_2CoO_4 (1.64, 1.73) > $\text{Sr}_2\text{CoO}_3\text{Br}$ (1.61, 1.65) > $\text{Sr}_2\text{CoO}_3\text{Cl}$ (1.53, 1.60) > $\text{Sr}_2\text{CoO}_3\text{F}$ (1.50, 1.56) V vs. HRE which indicates that $\text{Sr}_2\text{CoO}_3\text{F}$ is the most active electrode among the studied catalysts under static and steady-state conditions. Moreover, $\text{Sr}_2\text{CoO}_3\text{F}$ demonstrates long-term stability and remarkably less charge transfer resistance ($R_{ct} = 36.8 \text{ ohm}$) than the other oxyhalide counterparts during the OER. The doping of the perovskites with halide ions particularly the fluoride-ion enhances the surface oxygen vacancy density due to electron withdrawal away from the Co-atom which improves the ionic and electronic conductivity as well as the electrochemical activity of the oxygen evolution in alkaline solution.

Keywords: strontium cobalt oxyhalides; electrocatalyst; oxygen evolution reaction; alkaline solution



Citation: Ghanem, M.A.; Amer, M.S.; Al-Mayouf, A.M.; Arunachalam, P.; Weller, M.T. Halide-Doping Effect of Strontium Cobalt Oxide Electrocatalyst and the Induced Activity for Oxygen Evolution in an Alkaline Solution. *Catalysts* **2021**, *11*, 1408. <https://doi.org/10.3390/catal11111408>

Academic Editor: Yongjun Feng

Received: 17 October 2021

Accepted: 16 November 2021

Published: 20 November 2021

Publisher's Note: MDPI stays neutral with regard to jurisdictional claims in published maps and institutional affiliations.



Copyright: © 2021 by the authors. Licensee MDPI, Basel, Switzerland. This article is an open access article distributed under the terms and conditions of the Creative Commons Attribution (CC BY) license (<https://creativecommons.org/licenses/by/4.0/>).

1. Introduction

One of the most scientific challenges in energy conversion technologies is the discovery of cost-effective, highly active electrodes to implement the key electrochemical oxygen evolution (OER) and oxygen reduction reactions (ORR) in direct-solar and electricity-driven water splitting, fuel cells, and metal-air batteries [1–4]. However, the electrochemical oxygen evolution reaction (OER) in alkaline solution occurs through multistep proton-coupled electron transfers ($4\text{OH}^- \rightarrow 2\text{H}_2\text{O} + 4\text{e}^- + \text{O}_2$ in alkaline media) and it is kinetically slow [5,6], therefore, the development of highly active, abundant, and low-cost catalysts for water oxidation is one of the main tasks for large scale applications [7–9].

Among the non-precious metal-based catalysts replacements, perovskite-based materials (ABO_3) have shown good activity as bifunctional electrocatalysts for oxygen evolution (OER) and oxygen reduction (ORR) owing to good cation ordering, which boosts the mobility of oxygen ions for enhanced catalytic performance [10–12]. Furthermore, their composition, crystal structure, and morphology can be designed to further enhance their electronic and catalytic activities [13,14]. There has been much effort to identify appropriate

A- and B-site elements as well as the anions for perovskite structures (ABO_3) that could replace and offer higher catalytic performance for ORR and OER [15–21]. Within this context, the structural investigations of perovskites have shown that the weakening of the metal-oxygen bond by fully or partial substitution of the B-site enhances the ionic and electronic conductivity as well as the activity of OER and ORR [22–25]. Consequently, the oxygen vacancy density, as well as the valence and concentration of the B-cation, are changed within the structure improving the electronic properties and enhancing the catalytic activity [26,27]. Within this context, the doping of cobalt [28] or nickel [29] within the iron-molybdenum-based perovskite structure improves the electrochemical activity for the ORR in solid oxide fuel cell applications. The second strategy to achieve the desired chemical and physical properties of perovskite oxide is by partially exchanging the O-sites in the ABO_3 perovskite structure with anions such as Cl^- [30,31], N^{3-} [32], F^- [33,34], or S^{2-} [35]. The incorporation of such anions into the perovskite structure may decrease the coulombic force between oxygen and the B-site atom which promotes the lattice oxygen activity and migration [34,36]. Furthermore, due to the structural versatility of the perovskite family, layered perovskites and double perovskites have attracted more attention as competitive candidates as bifunctional catalysts in ORR and OER catalysis [37–40]. Takeguchi et al. reported a reversible oxygen electrocatalyst consisting of layered perovskite of $LaSr_3Fe_3O_{10}$ [41] and Grimaud et al. fabricated double perovskite composed of cobalt-type ($PrBaCo_2O_{5+d}$) that exhibited even higher OER performance than the BSCF type [42]. Previously, our group reported the effect of chloride-doping of a layered iron oxy-chloride perovskite (Sr_2FeO_2Cl) that exhibited good oxygen electrocatalytic activity as well as a bifunctional OER/ORR electrocatalyst. Interestingly, the lower the oxygen and higher chloride content in this type of oxy-chloride perovskite materials significantly enhanced the OER/ORR activity [38]. Within this context, Miyahara et al. reported a highly active OER electrocatalyst with layered cobalt perovskite oxychlorides of Sr_2CoO_3Cl and $Sr_3Co_2O_5Cl_2$. They attributed the high OER/ORR electrocatalytic activity to the incorporation of a chloride anion into oxygen sites that upshifted the O p-band center of the Fermi level [39]. Nevertheless, the research on perovskites anion-doping and the influence on the structural oxygen deficiency and activity for oxygen evolution reaction is limited, therefore, this work reports a comparative and systematic investigation of the effect of halide ions doping (F^- , Cl^- , and Br^-) on strontium cobalt layered perovskite (Sr_2CoO_4) electrocatalyst and the induced performance of the electrochemical activity towards OER in an alkaline solution compared to the parent oxide.

2. Results and Discussion

2.1. Structure and Morphology of the $Sr_2CoO_{3-x}H_x$ Catalysts

Figure 1 shows the XRD patterns of the crystal structures of Sr_2CoO_4 , Sr_2CoO_3F , Sr_2CoO_3Cl , and Sr_2CoO_2Br catalysts. All the prepared oxyhalides showed identical peaks of the desired compounds, confirming that the resultant oxyhalides had a layered perovskite structure, except for a minor 5.6% impurity assigned to $Sr_6Co_5O_{15}$ and other unidentified impurities [42–45]. The XRD results reveal the main crystal structure phase has a tetragonal structure that is equivalent to the Sr_2CoO_4 RP-type structure with a space group of $I4/mmm$ with the Co atom in octahedral coordination with six oxygen/halide anions (JCPDS ICDD card NO. 01-070-3734). The oxygen/halide anions are disordered at the apical sites and the Sr cation occupies an interstitial space of the eight corner-sharing of the octahedral Co atom [24,25,46].

Figure 2 presents the SEM images of the surface morphology of the prepared Sr_2CoO_4 , Sr_2CoO_3F , Sr_2CoO_3Cl , and Sr_2CoO_3Br catalysts showing that the catalysts have similar micrometer-sized irregular shaped particles, with no significant difference in the surface morphology observed for the oxyhalides from the Sr_2CoO_4 parent catalyst. As an example, the SEM-EDX mapping images of the Sr_2CoO_3F catalyst are shown in Figure 3 which reveals the uniform distribution of the constituent elements of Sr, Co, O, and F throughout the sample.

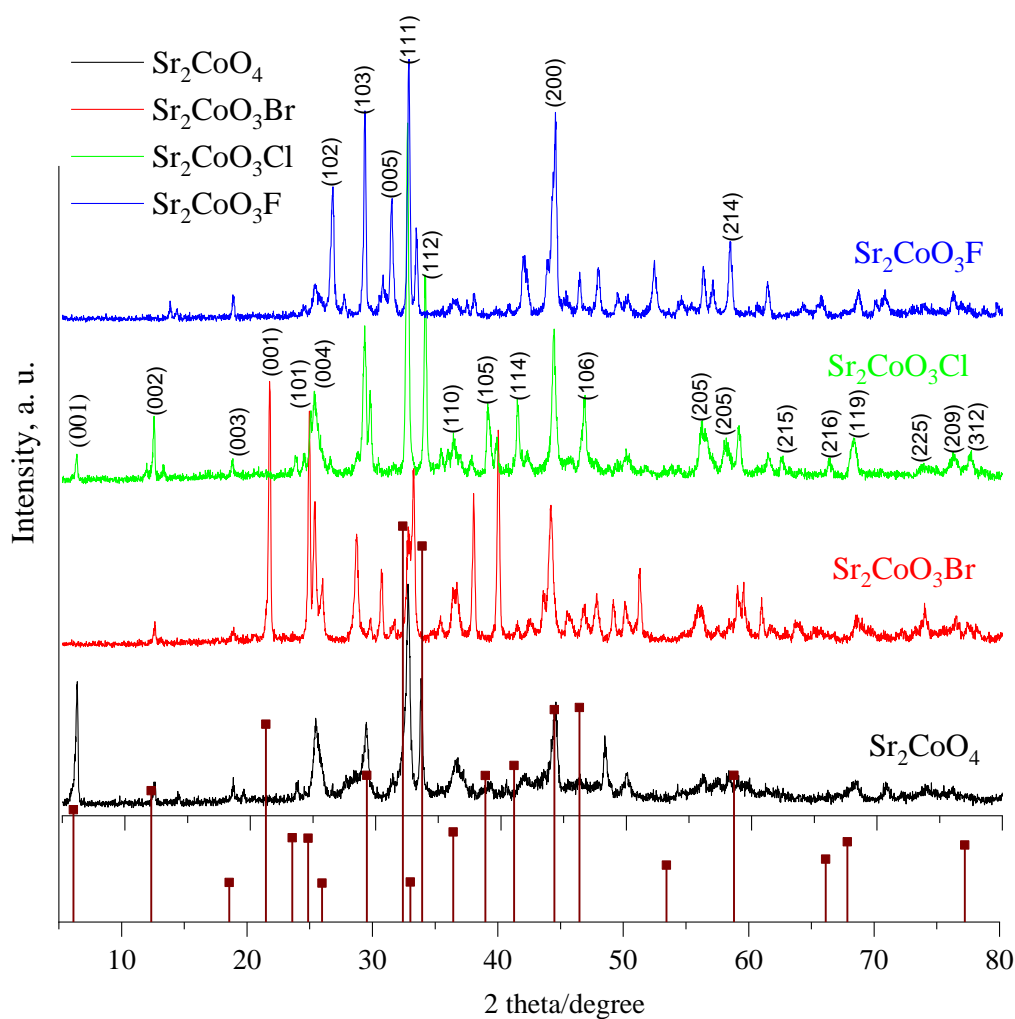


Figure 1. XRD patterns of strontium cobalt oxyhalide catalysts.

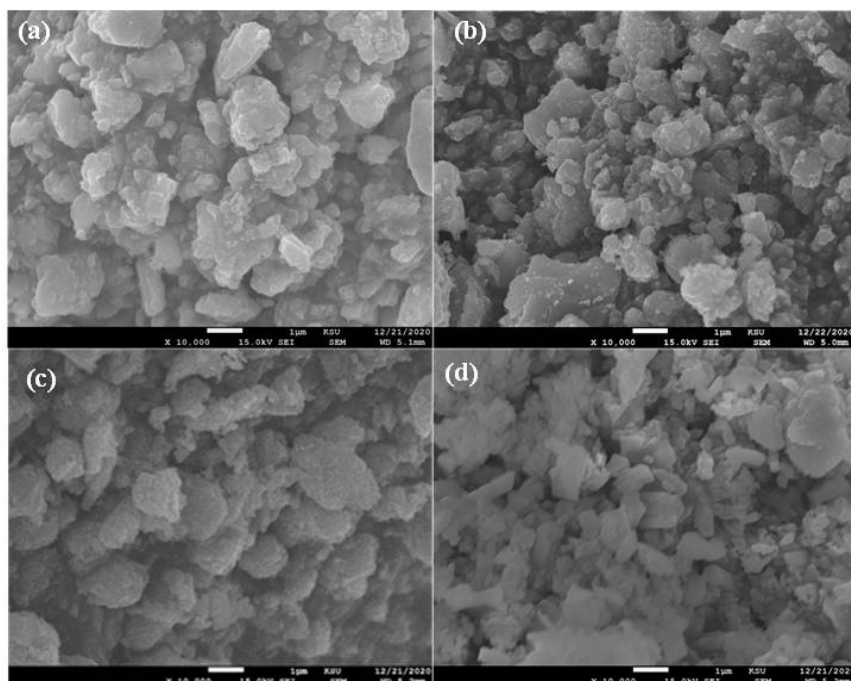


Figure 2. SEM images of (a), (b) $\text{Sr}_2\text{CoO}_3\text{F}$, (c) $\text{Sr}_2\text{CoO}_3\text{Cl}$, and (d) $\text{Sr}_2\text{CoO}_3\text{Br}$ catalysts.

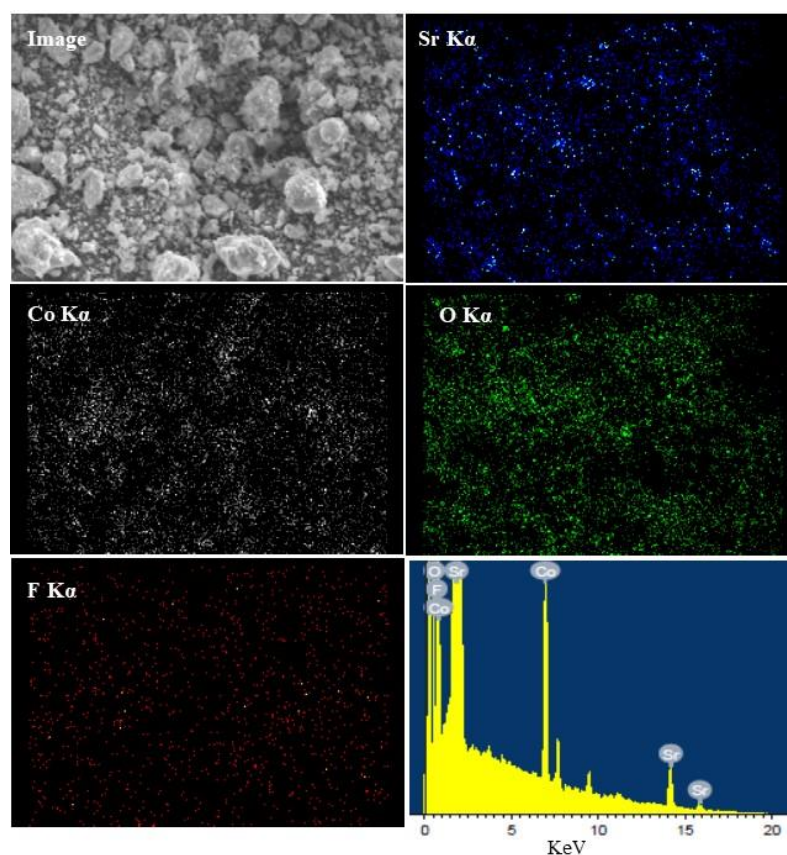


Figure 3. SEM-EDX composition map analysis of $\text{Sr}_2\text{CoO}_3\text{F}$ catalyst.

Table 1 SEM-EDX elemental composition analysis of the strontium cobalt oxyhalide catalysts in comparison to the parent oxide of Sr_2CoO_4 .

Table 1. The EDX elemental composition analysis of the strontium cobalt oxyhalide catalysts and the parent oxide of Sr_2CoO_4 .

Catalyst	Sr wt. % $\pm 2.0\%$	Co wt. % $\pm 2.0\%$	O wt. % $\pm 2.0\%$	H wt. % $\pm 2.0\%$
Sr_2CoO_4	59.06	19.64	21.30	–
$\text{Sr}_2\text{CoO}_3\text{F}$	58.18	19.56	15.93	6.33
$\text{Sr}_2\text{CoO}_3\text{Cl}$	55.15	18.55	15.13	11.17
$\text{Sr}_2\text{CoO}_3\text{Br}$	49.63	16.70	13.60	20.07

The elemental composition of the overall oxyhalides was determined by SEM-EDX mapping analysis and Table 1 summarises the elemental composition analysis of the strontium cobalt oxyhalide catalysts in addition to the parent oxide of Sr_2CoO_4 . The results revealing good agreement between the EDX elemental analysis and the molecular formula of Sr_2CoO_4 , $\text{Sr}_2\text{CoO}_3\text{F}$, $\text{Sr}_2\text{CoO}_3\text{Cl}$, and $\text{Sr}_2\text{CoO}_3\text{Br}$, except for an impurity within 2.0 wt.% attributed to the unidentified strontium cobalt oxide phase as confirmed by X-ray analysis.

Furthermore, Figure S1 shows the wide XPS spectra of the oxyhalide catalysts that reveal the surface chemical functionality and the oxygen atom bonding upon incorporating F^- , Cl^- or Br^- anions. The XPS wide spectra clearly show the peaks for the C 1s that commonly originates from the carbon surface contamination and the main constituent elements of Sr 3d, Co 2p, and O 1s. Figure 4 shows the deconvoluted core spectra analysis of the O 1s peak for the $\text{Sr}_2\text{CoO}_3\text{F}$, $\text{Sr}_2\text{CoO}_3\text{Cl}$, $\text{Sr}_2\text{CoO}_3\text{Br}$, and parent Sr_2CoO_4 while Table 2 reports the deconvoluted O 1s peaks binding energy and oxygen bonding ratio values of the studied oxyhalide catalysts. The O 1s fitted core spectra in Figure 4 reveal the

presence of a peak at lower binding energy (peak 1) that can be assigned to the O^{2-} anion of the lattice oxygen and the peak in the middle is related to the surface O^{1-} ions (peak 2), while the peak at higher binding energy (peak 3) is due to the chemically adsorbed oxygen species (O^{chem}) at the surface [47,48]. However, the O 1s spectrum of the parent Sr_2CoO_4 catalyst (Figure 4d) can only be fitted by two peaks that are assigned for O^{2-} anion (peak 1) and O^{1-}/O^{chem} (peak 2), possibly because of a small amount of chemically adsorbed oxygen species. From the data in Table 2 and upon the incorporation of halide ions, the overall peaks' binding energy is shifted to lower values in the order $F^- > Cl^- > Br^-$ which indicates a weaker Co-O bonding due to withdrawn the electron density away from the Co-atom, consequently enhances the lattice oxygen (O^{2-}) reactivity and reduces the activation energy required for O^{2-} activation [47–49]. Moreover the O 1s fitted peaks' area ratio of $[O^{1-}/O^{2-}]$ as well as the $[(O^{1-} + O^{chem})/O^{2-}] / O^{2-}$ were much higher in case of Sr_2CoO_3F (3.1, 13.20) than for Sr_2CoO_3Cl (2.9, 3.83), Sr_2CoO_3Br (1.28, 1.91) and the parent Sr_2CoO_4 (0.63, 0.63) catalysts, respectively. Therefore, the doping of halide ions particularly fluoride ion enhanced the O^{1-} and O^{chem} site concentration that directly related to the density of the surface oxygen vacancy defects [48,49].

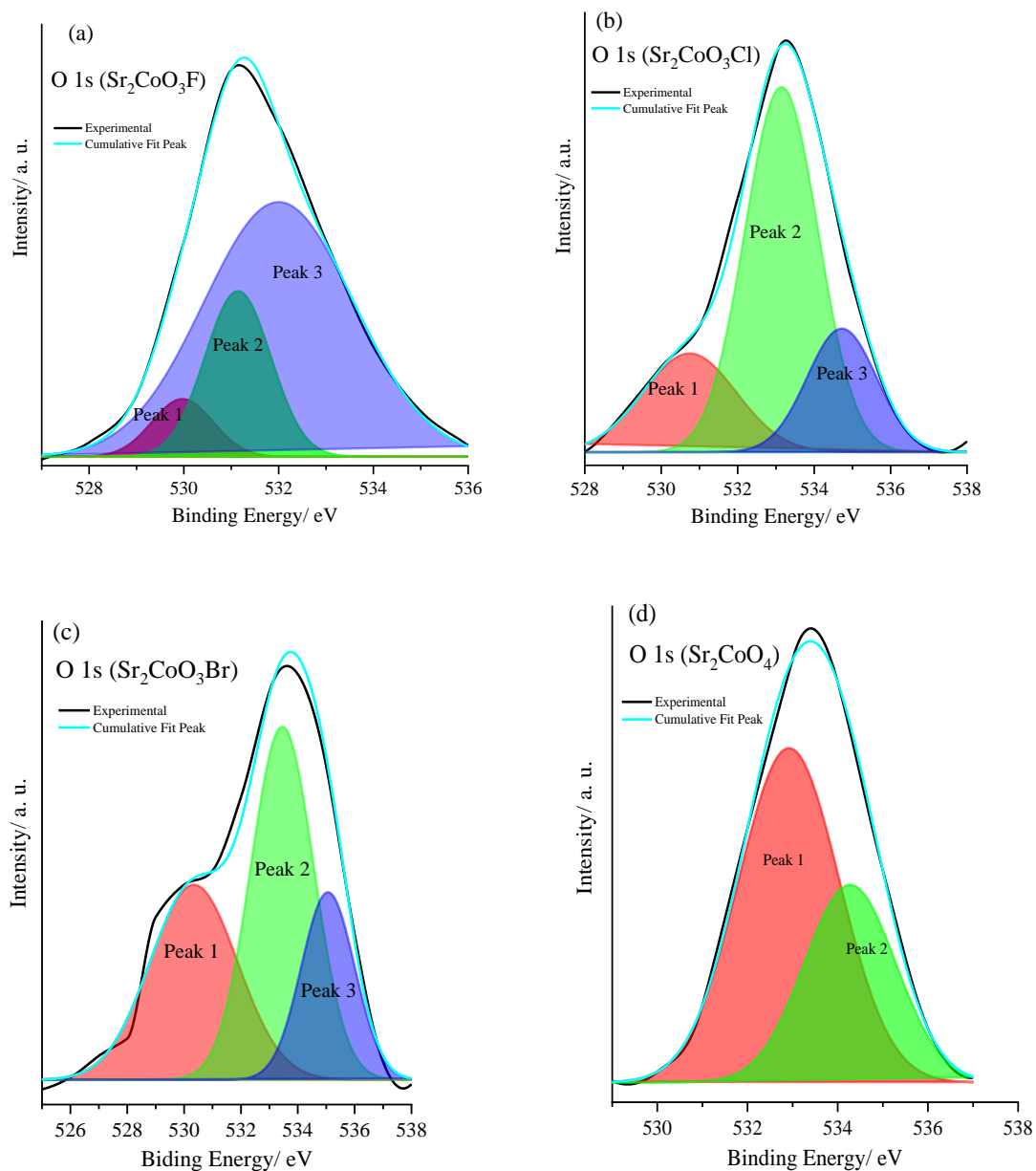


Figure 4. The core-level of O 1s spectra of (a) Sr_2CoO_3F , (b) Sr_2CoO_3Cl , (c) Sr_2CoO_3Br and (d) parent Sr_2CoO_4 catalyst.

Table 2. Analysis values of the deconvoluted O 1s peaks of the oxyhalide catalysts.

Catalyst	Peak BE (O ²⁻)/eV	Peak 1 Area %	Peak 2 (O ¹⁻)/eV	Peak Area %	Peak 3 (O ^{chem})/eV	Peak 3 Area %	[O ¹⁻ / O ²⁻]	[O ¹⁻ + O ^{chem} /O ²⁻]
Sr ₂ CoO ₄	532.90	61.4	534.2	38.6	–	–	0.63	0.63
Sr ₂ CoO ₃ Br	530.34	34.3	533.45	43.9	535.06	21.8	1.28	1.91
Sr ₂ CoO ₃ Cl	530.74	20.7	533.14	60.1	534.72	19.2	2.90	3.83
Sr ₂ CoO ₃ F	529.96	6.7	531.14	20.8	532.01	72.5	3.10	13.20

2.2. Electrocatalytic Activity of Cobalt Oxyhalide Catalysts in OER

The electrochemical behavior and activity of the produced strontium cobalt oxyhalide (Sr₂CoO_{3-x}H_x) catalysts were evaluated for the OER in 1.0 M NaOH by cyclic voltammetry. The catalyst particles were uniformly deposited as thin films on the carbon paper electrodes via electrophoretic deposition at predefined catalyst loading. Figure 5a shows cyclic voltammograms (CV) at 20 mV s⁻¹ of the Sr₂CoO_{3-x}H_x (x = 1) compared to carbon paper in the narrow potential window in 1.0 M NaOH. The blank carbon paper electrode (grey line) shows the standard capacitance CV, while the oxyhalide voltammograms exhibit the well-known shape of the Faradic cobalt redox Co(II)/Co(III) system. Although the oxyhalide catalysts have almost similar cobalt wt.% (Table 1 above), the CV indicates that the Sr₂CoO₃F electrode exhibits a significantly higher electrochemical Co(II)/Co(III) redox current than Sr₂CoO₄, Sr₂CoO₃Cl, and Sr₂CoO₃Br, suggesting that the Sr₂CoO₃F electrode has a higher electroactive surface of Co(II)/Co(III) sites. Figure 5b compares the linear sweep voltammetry (LSV) at 20 mV s⁻¹ for the strontium cobalt oxyhalide (Sr₂CoO_{3-x}H_x) compared to the parent Sr₂CoO₄ in 1.0 M NaOH electrolyte at a catalyst loading of 0.8 mg/cm². In the case of the oxyhalides electrodes, significant catalytic activity towards the OER was observed, as evidenced by less positive onset potential and the higher current density compared to the pristine Sr₂CoO₄ (black line) catalyst. Table 3 reports the OER catalyst characteristic parameters of onset potential (the potential at 1.0 mA/cm²), the potential at a current density of 10 mA cm⁻² ($\eta_{10\%}$) that corresponds to 10% solar to the energy efficiency of the cobalt oxyhalides. The incorporation of halide anions of F⁻, Cl⁻, or Br⁻ into the Sr₂CoO₄ substrate enhanced the OER, with the onset potential shifting to less positive in the order of F⁻ (1.50) < Cl⁻ (1.52) < Br⁻ (1.61) < Sr₂CoO₄ (1.64) V vs. HRE. Moreover, the (η_{10}) values similarly decrease as Sr₂CoO₄ (1.73) > Sr₂CoO₃Br (1.67) > Sr₂CoO₃Cl (1.60) > Sr₂CoO₃F (1.56) V, indicating that Sr₂CoO₃F is the most active electrode among the studied catalysts, presumably due to its higher electroactive surface area and/or conductivity as shown by the impedance analysis below. Moreover, the electrochemical behavior of the oxyhalides catalysts was investigated under steady-state conditions using rotating disk electrode (RDE) of glassy carbon, and the results of LSVs at a rotation speed of 1600 rpm and 10 mV s⁻¹ are shown in Figure S2. The RDE results and as shown in Table 3 revealed no significant change in the values of the OE onset potential and ($\eta_{10\%}$) under steady-state condition confirming the electrode kinetic is the predominant during oxygen evolution reaction. Moreover, a comparable activity trend towards the oxygen evolution was achieved confirming the Sr₂CoO₃F catalyst is the most active under either static or steady-state conditions.

To gain more insight on the enhanced OER activity of the oxyhalide catalysts, Tafel plots were used to examine the catalysis kinetics for the OER and are plotted in Figure 5c as extracted from the LSV shown in Figure S2 (Supporting Information) that performed at a scan rate of 10 mV s⁻¹ and rotation rate of 1600 rpm. The Tafel plots describe the relationship between the overpotential and the logarithm of the current (I), which can provide important information about water oxidation including the electronic and geometric enhancement in the activity of the electrocatalyst [49]. As shown in Table 3, the Tafel slope values decrease in the order of Sr₂CoO₄ (110 mV/dec) > Sr₂CoO₃Br (103 mV/dec) > Sr₂CoO₃Cl (98 mV/dec) > Sr₂CoO₃F (88 mV/dec), indicating that the OER kinetics are

more favourable at the $\text{Sr}_2\text{CoO}_3\text{F}$ electrode than $\text{Sr}_2\text{CoO}_3\text{Cl}$, $\text{Sr}_2\text{CoO}_3\text{Br}$ and the pristine Sr_2CoO_4 catalyst.

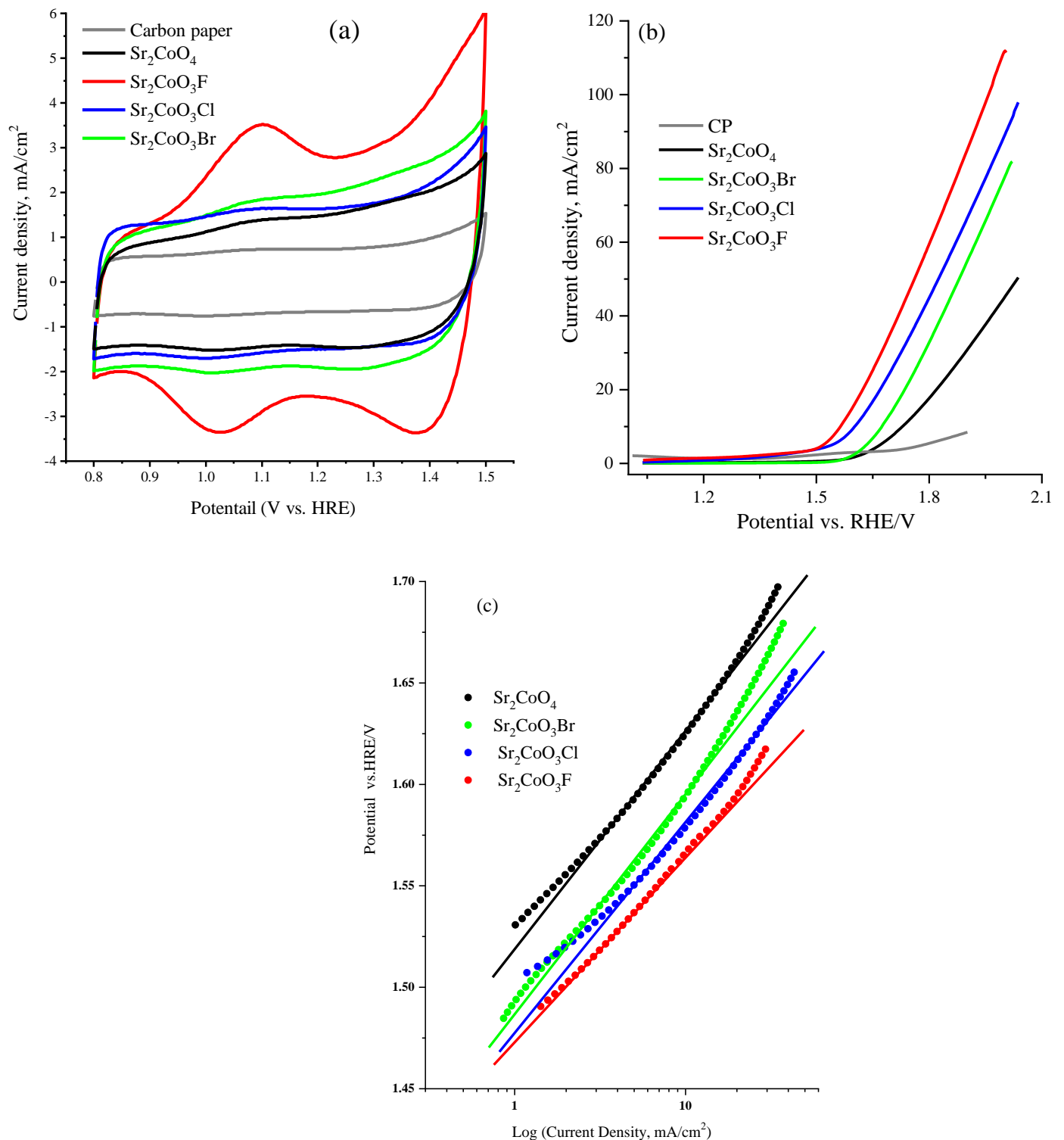


Figure 5. (a) cyclic voltammetry in the narrow potential window at 20 mV s^{-1} for the strontium cobalt oxy-halide ($\text{Sr}_2\text{CoO}_{3-x}\text{H}_x$, $\text{H} = \text{F}, \text{Cl}$ or Br and $x = 1$) catalysts in 1.0 M NaOH electrolyte and catalyst loading of 0.8 mg/cm^2 , (b) linear sweep voltammetry within OER region at 20 mV s^{-1} for the strontium cobalt oxyhalides catalysts in 1.0 M NaOH electrolyte and catalyst loading = 0.8 mg cm^{-2} , and (c) Tafel slopes of the oxyhalides catalysts as extracted from LSV shown in Figure S2 (supporting Information) and performed at a scan rate of 10 mV s^{-1} and rotation rate of 1600 rpm .

Table 3. The oxygen evolution onset potential and overpotential at a current density of 10 mA/cm² ($\eta_{10\%}$) and Tafel slope of the strontium cobalt oxyhalides catalysts.

Catalyst	Onset Potential \pm 0.005 vs. RHE/ V	Onset Potential \pm 0.005 vs. RHE/ V (RDE = 1600 rpm)	Potential at 10 mA/cm ²	Potential at 10 mA/cm ² (RDE = 1600 rpm)	Tafel slope, mV/dec (at 1.0 mV s ⁻¹ Using GCE)
Sr ₂ CoO ₃ F	1.50	1.45	1.56	1.56	88
Sr ₂ CoO ₃ Cl	1.53	1.49	1.60	1.57	98
Sr ₂ CoO ₃ Br	1.61	1.51	1.65	1.60	103
Sr ₂ CoO ₄	1.64	1.55	1.73	1.65	110

Electrochemical impedance spectra (EIS) analysis was also employed to evaluate the charge carrier transfer resistance during the OER for the oxyhalide catalysts of Sr₂CoO₃F, Sr₂CoO₃Cl, and Sr₂CoO₃Br compared to pristine Sr₂CoO₄ catalyst. Figure 6 presents typical Nyquist plots of the impedance data obtained for the strontium cobalt oxyhalide (Sr₂CoO_{4-x}H_x) compared to the pristine Sr₂CoO₄ catalyst at 1.55 V versus HRE and within the frequency range of 0.01 to 1.0 MHz with a 20-mV s⁻¹ amplitude in 1.0 M NaOH. The Nyquist diagram of the oxyhalide electrodes can be fitted to the standard R_s/Q₁/R_{ct} equivalent circuit illustrated in the inset of Figure 6, where the R_s is the solution resistance, R_{ct}, the charge transfer resistance, and Q₁ is the double-layer capacitance at the catalyst/electrolyte interface. The impedance parameters obtained from the fitted equivalent circuit of the oxyhalide catalyst are reported in Table 3. The most significant characteristic observed in Figure 6 and Table 4 is the radii of the arc that related to the charge transfer resistance (R_{ct}) on the EIS Nyquist plots of Sr₂CoO₃F (36.8 Ω) is significantly smaller compared to Sr₂CoO₃Cl (52.9 Ω), Sr₂CoO₃Br (128.5 Ω) and pristine Sr₂CoO₄ (296.1 Ω), catalysts, suggesting that the Sr₂CoO₃F catalyst possesses a remarkably lower charge transfer resistance (R_{ct}) at the catalyst/electrolyte interface during the OER.

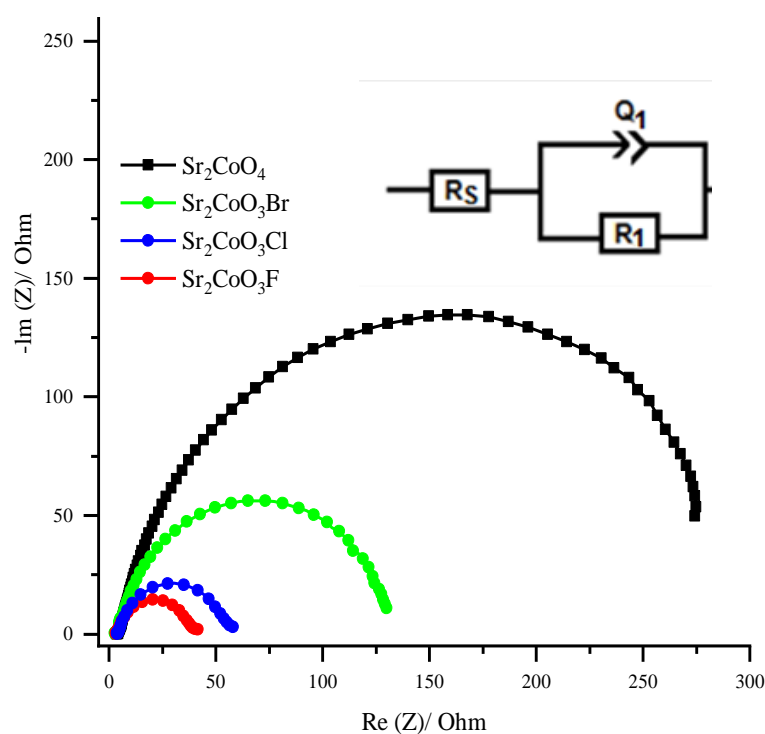


Figure 6. EIS Nyquist diagram and equivalent circuit of the oxyhalides and parent Sr₂CoO₄ electrodes (loading of 0.8 mg/cm²) in 1.0 M NaOH solution at 1.55 V versus HRE and within the frequency range of 0.01 to 1.0 MHz with a 20 mV amplitude. The solid lines are the fitted curves and the symbols are representing the experimental data.

Table 4. Impedance parameter values derived from the fitting of the equivalent circuit for the impedance spectra of the oxyhalides catalysts recorded in 1.0 M NaOH solution at 1.55 V vs. HRE and within the frequency range of 0.01 to 1.0 MHz with a 20 mV amplitude.

Catalyst	R_s (ohm)	Q_1 (mF)	R_1 (ohm)
Sr_2CoO_4	4.18	21.680	296.1
Sr_2CoO_3Br	4.37	21.890	128.5
Sr_2CoO_3Cl	4.17	22.310	52.9
Sr_2CoO_3F	4.23	38.300	36.8

Furthermore, the values of the double-layer capacitance (Q_1) indicate that the Sr_2CoO_3F catalyst shows higher capacitance than the other oxyhalide electrodes, which agrees with the results obtained from linear sweep voltammetry above. The ISE analysis implies that the Sr_2CoO_3F catalyst accelerates the charge transfer kinetics and acts as a highly effective OER catalyst. The enhanced electrochemical oxygen evolution performance of the oxyhalides over parent Sr_2CoO_4 catalyst can be attributed to the doping of Cl^- , Br^- and in particular the F^- ions enhanced the O^{1-} and O^{chem} sites concentration that improve the ionic and electronic conductivity as well as the electrochemical activity.

The long-term stability of the strontium cobalt oxyhalide ($Sr_2CoO_{3-x}H_x$) catalysts during OER in alkaline solution was investigated by chronoamperometry and chronopotentiometry measurements. Figure 7 presents the chronoamperometric curves of the Sr_2CoO_4 , Sr_2CoO_3F , Sr_2CoO_3Cl , and Sr_2CoO_3Br catalysts in 1.0 M NaOH (pH = 14) at a constant potential of 1.65 V vs. HRE for 12 h, showing that the Sr_2CoO_3F catalyst exhibits outstanding stability with no obvious current density decrease and maintained about 95% of the oxygen evolution activity after 12 h of electrolysis.

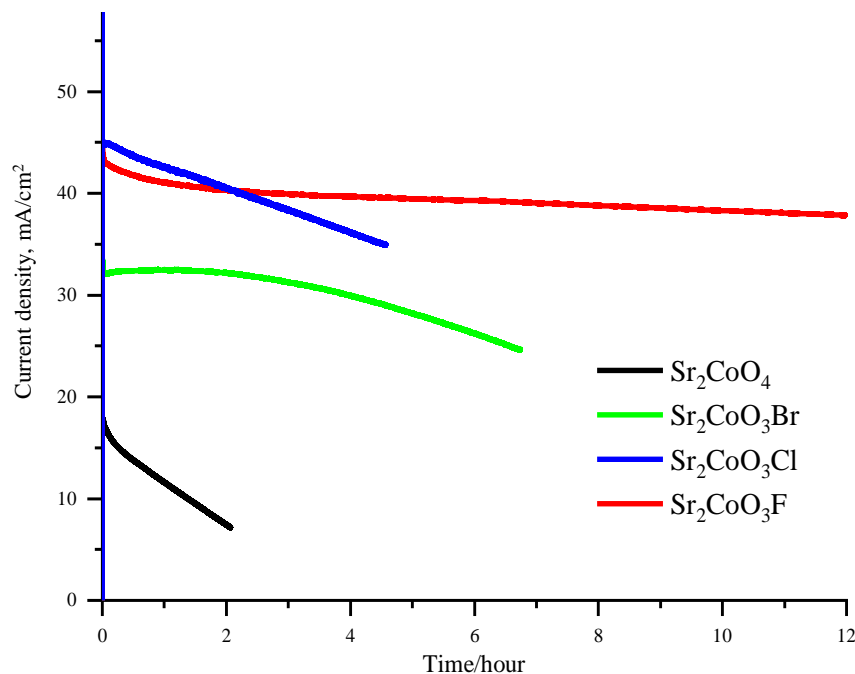


Figure 7. Chronoamperometric curves of the Sr_2CoO_4 , Sr_2CoO_3F , Sr_2CoO_3Cl , and Sr_2CoO_3Br catalysts (0.8 mg/cm^2) in 1.0 M NaOH (pH = 14) at constant potential of 1.65 V vs. HRE.

In contrast, Sr_2CoO_3Cl , Sr_2CoO_3Br , and Sr_2CoO_4 suffer reduced activity and the current density decreased from 44.8 to 35 mA cm^{-2} , 32.2 to 24.6 mA cm^{-2} , and 18.3 to 7.5 mA cm^{-2} , respectively, after only 4 h or less during electrolysis. Presumably, during the long-term stability test in alkaline solution and under applied potential, the halide-doped strontium cobalt oxide catalysts are partially converted to oxyhydroxides due to

the intercalation of OH^- groups with the fluoride-doped catalyst having the most stable $\text{O}^{2-}/\text{OH}^-/\text{F}^-$ coordination and bonding with Co atom due to the stronger electron affinity of fluoride ion [48,49]. However, more work is required to understand the oxyhalide catalysts' structural changes and the corresponding intrinsic activity during prolonged electrolysis in alkaline solution. In conclusion, the electrochemical measurements suggest that the $\text{Sr}_2\text{CoO}_3\text{F}$ is the most active and stable catalyst for OER applications among the studied strontium cobalt oxyhalide catalysts.

2.3. Electrochemical Performance of the $\text{Sr}_2\text{CoO}_3\text{F}$ Catalyst

The $\text{Sr}_2\text{CoO}_3\text{F}$ catalyst activity during OER in alkaline solution was optimized by studying the catalyst loading effect, NaOH concentration, and long-term stability at a predefined constant potential or current density. Figure 8a shows the linear sweep voltammograms at 20 mV s^{-1} of the $\text{Sr}_2\text{CoO}_3\text{F}$ catalyst at different catalyst loadings. Moreover, Figure 8b illustrates the effect of the catalyst loading on the potential at 10 mA/cm^2 (black line) and the OER current density achieved at 1.8 V vs. HRE (red line). From Figure 8b, the $\text{Sr}_2\text{CoO}_3\text{F}$ catalyst loading around 0.8 mg/cm^2 is optimal to achieve the best OER activity, that is, the smallest potential at 10 mA/cm^2 and the highest current density at 1.8 V vs. HRE. In addition, Figure 8c illustrates the LSV at 20 mV s^{-1} of the $\text{Sr}_2\text{CoO}_3\text{F}$ catalyst (at 0.8 mg loading) in different concentrations of NaOH electrolyte, showing that the OER onset potential is significantly shifted to a less positive potential from 0.66 to 0.52 V vs. SCE by increasing the NaOH from 0.1 to 5.0 M , respectively. In addition, the OER current density substantially increased at a more positive potential indicating the enhancement of OER in concentrated alkaline solution. The oxygen evolution at a less positive potential in concentrated alkaline solution could be attributed to the Nernst effect and the current density enhancement due to an increase of OH^- ion concentration at the catalyst/electrolyte interface. EIS analysis was also employed to evaluate the charge carrier transfer resistance of the most active oxyhalides of $\text{Sr}_2\text{CoO}_3\text{F}$ at the different applied potentials. Figure 8d presents typical Nyquist plots of the impedance data obtained for the $\text{Sr}_2\text{CoO}_3\text{F}$ at $\text{Sr}_2\text{CoO}_3\text{F}$ at different applied potential and frequency ranges of 0.01 to 1.0 MHz with a 20 mV amplitude, showing that the radii of the arc in the EIS Nyquist plots of $\text{Sr}_2\text{CoO}_3\text{F}$ decrease with the increasing applied potential from 1.55 to 1.62 , suggesting that the charge transfer resistance of OER at the $\text{Sr}_2\text{CoO}_3\text{F}$ catalyst decreases with increasing applied potential indicating higher OER performance. Furthermore, Table 5 reports the impedance parameter values of solution resistance (R_s), double-layer capacitance (Q_1), and charge transfer resistance (R_1) derived from the fitting of the equivalent circuit (shown in Figure 8d inset) for the impedance spectra at a different applied potential of the $\text{Sr}_2\text{CoO}_3\text{F}$ catalyst, indicating that charge transfer resistance (R_1) significantly decreased from 36.8 to 4.34 ohm by increasing the applied potential from 1.55 to 1.62 V , confirming the enhancement of the charge transfer and the acceleration of the OER kinetics at the $\text{Sr}_2\text{CoO}_3\text{F}$ catalyst.

Table 5. Impedance parameter values derived from the fitting of the equivalent circuit for the impedance spectra of $\text{Sr}_2\text{CoO}_3\text{F}$ at different applied potential recorded in 1.0 M NaOH solution.

Potential (V) vs. HRE	R_s (ohm)	Q_1 (mF)	R_1 (ohm)
1.55	4.23	38.300	36.8
1.57	4.22	38.600	15.9
1.58	4.13	41.750	10.40
1.60	4.19	41.760	6.30
1.62	4.16	41.510	4.34

Finally, Figure 9 shows the chronoamperometry and chronopotentiometry at a predefined applied potential and current density during the prolonged OER at the $\text{Sr}_2\text{CoO}_3\text{F}$ catalyst in 1.0 M NaOH. The $\text{Sr}_2\text{CoO}_3\text{F}$ catalyst exhibits long-term stability with an almost stable current and potential during water oxidation in an alkaline solution. The catalyst

recorded a potential of 1.58 V vs. HRE to achieve a current density of 10 mA/cm² that is required for 10% efficiency of solar to hydrogen production which outperforms the benchmarked catalysts prepared by other approaches.

For the evaluation of the Sr₂CoO₃F against the benchmark of perovskites and iridium oxide catalysts, Table S1 reports our strontium cobalt oxyhalides catalysts activities of OER onset overpotential and the overpotential required to achieve 10 mA/cm² current density ($\eta_{10 \text{ mA/cm}^2}$) in comparison to the benchmarking catalysts that reported in the literature. The Sr₂CoO₃F catalyst exhibits superior OER onset overpotential (270 mV) lower than that of well-known precious metal IrO₂ catalyst (320 mV) [S11] in an alkaline solution. Moreover, the Sr₂CoO₃F shows better OER activity than that of perovskite cobalt-based catalysts such as Sr₃Co₂O₅Cl₂ [S3] hydrated Sr₃Co₂O₅(OH)₂ [S1] and defected SrCo_{0.8}Fe_{0.5-x}O_{3- δ} [S5]. Finally, the catalysts the Sr₂CoO₃F catalyst reveal OER activity that is comparable to the catalysts of nickel–cobalt–fluoride [S6] and nickel–iron–oxyfluoride [S10].

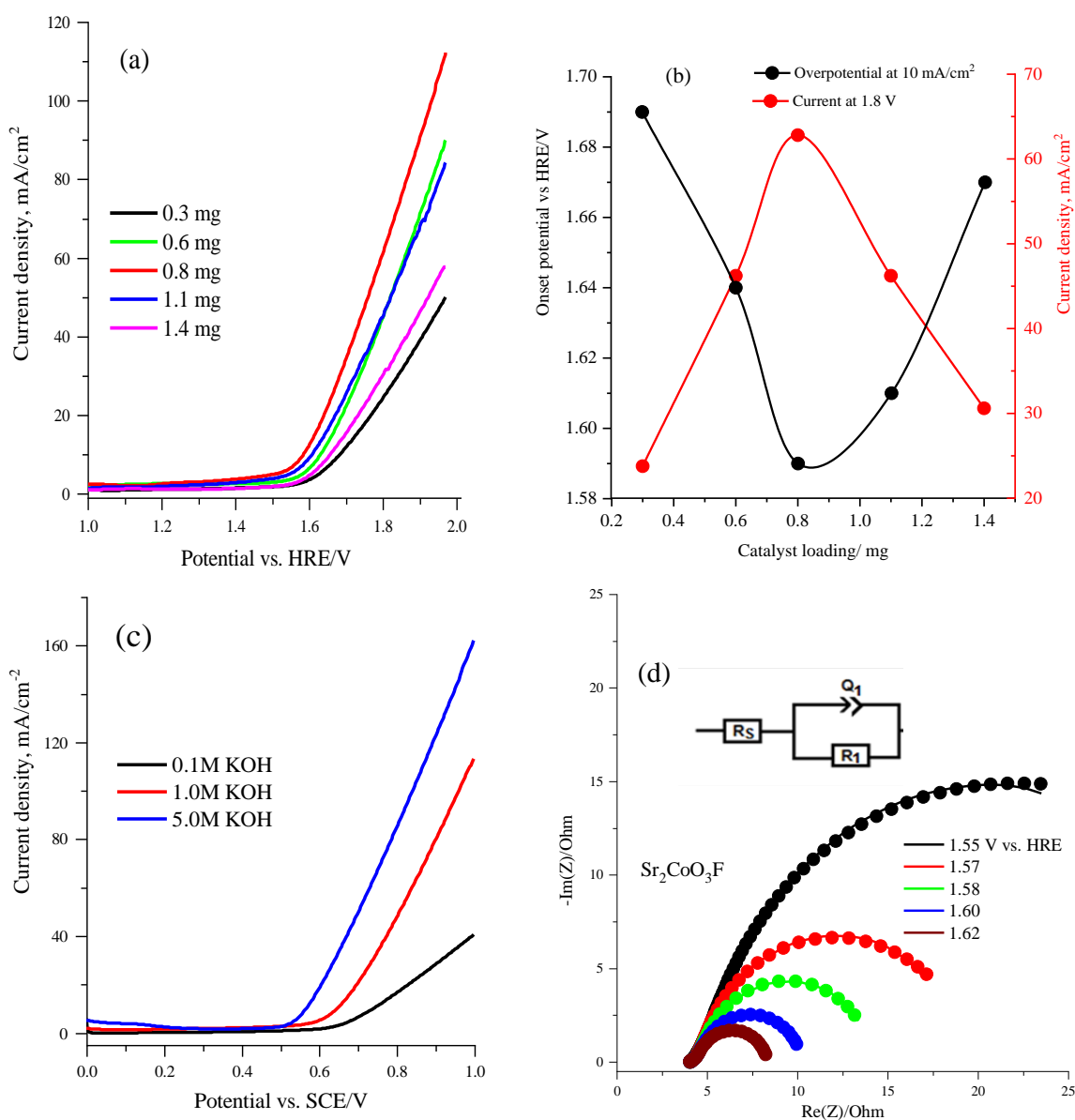


Figure 8. (a) LSV at 20 mVs⁻¹ for the Sr₂CoO₃F catalyst in 1.0 M NaOH electrolyte with different catalyst loading, (b) plot for the relation of the catalyst loading against the potential at 10 mA/cm² (black line) and the OER current density achieved at 1.8 V vs. HRE (red line), (c) the LSV at 20 mVs⁻¹ of the Sr₂CoO₃F catalyst (loading of 0.8 mg/cm²) in different concentration of NaOH electrolyte, and (d) EIS Nyquist diagram and equivalent circuit for the Sr₂CoO₃F catalyst at the different applied potential within the frequency range of 0.01 to 1.0 MHz and a 20 mV amplitude and in 1.0 M NaOH solution.

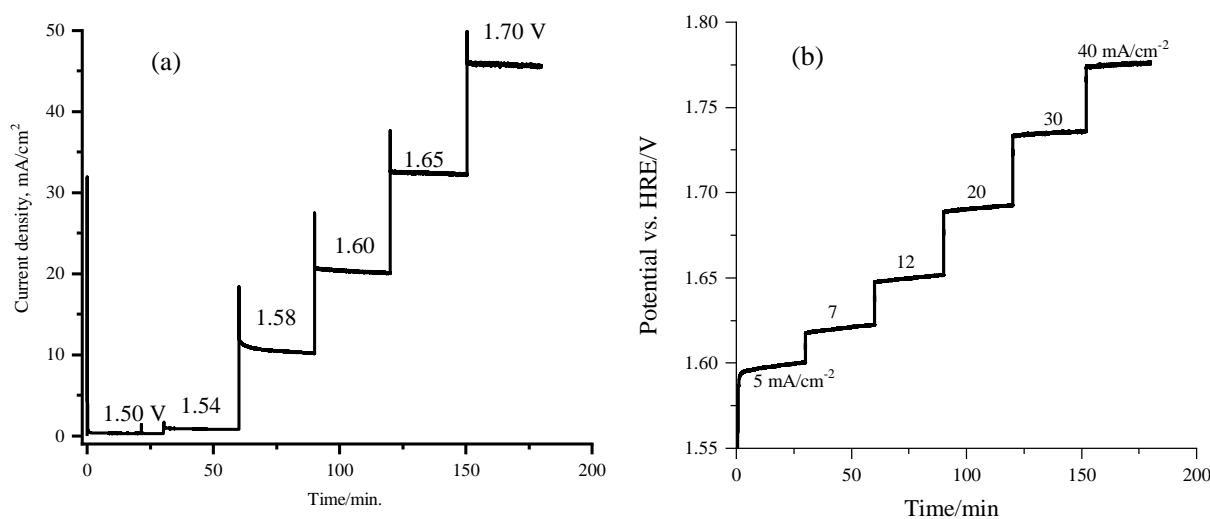


Figure 9. (a) chronoamperometry at different applied potential and (b) chronopotentiometry at a different applied current density of the Sr₂CoO₃F catalyst (loading 0.8 mg/cm²) in 1.0 M NaOH electrolyte during prolonged water oxidation.

3. Materials and Methods

3.1. Catalyst Preparation Characterizations

A set of the perovskite oxyhalides of strontium cobalt oxyhalides (Sr₂CoO_{3-x}H_x, where H = F, Cl, or Br, and x = 0 or 1; Sr₂CoO₄, Sr₂CoO₃F, Sr₂CoO₃Cl, and Sr₂CoO₂Br) were prepared by solid-phase synthesis following the method reported in the literature [45,46]. A stoichiometric molar ratio of SrCO₃ (99.9%, Aldrich, Dorset, UK), Co₃O₄ (99.9%, Kojundo Chemical Laboratory, Mölndal, Sweden), and the potassium precursor of chloride, bromide, or fluoride (Aldrich, 99.95%) were ground and heated at 850 °C under a nitrogen atmosphere in a platinum crucible for 24 days. The products were cooled to room temperature, reground, and heated to 550 °C for a further 12 h. The product was cooled to room temperature, reground, and stored for further characterization.

The crystallography and phase data of the fabricated catalysts were analyzed by powder X-ray diffraction (XRD, Rigaku Miniflex 600, Rigaku Corporation, Tokyo, Japan) using Cu K_α radiation. The surface morphology and elemental composition of the fabricated catalysts were examined by a scanning electron microscope (SEM; S-4800, Hitachi, Oberkochen, Germany) with a fitted energy dispersive X-ray spectrometer detector (EX350, Horiba).

3.2. Electrochemical Measurements

All electrochemical characterizations were performed using a potentiostat/galvanostat (Autolab PGSTAT302) electrochemical system in a three-electrode glass cell using 1.0 M NaOH (>99%, Loba Chemie PVT Ltd., Mumbai, India) electrolyte. Carbon paper (SIGRACET[®], GDL-24BC, SGL CARBON SE, Bonn, Germany) or glassy carbon rotating disk electrode (GC-RDE, 3 mm diameter, Metrohm, Herisau, Switzerland) was employed as a working electrode, and the saturated calomel electrode (SCE) and Pt-mesh (0.5 × 1.0 cm²) were used as the reference and counter electrodes, respectively. The oxyhalide catalyst was deposited by electrophoretic deposition (EPD) on the CP substrate. Briefly, the catalyst powder (15 mg) was dispersed in 15 mL acetone containing 40 mg iodine using an ultrasonic probe for 10 min. The electrophoretic deposition cell was constructed using a 50 mL glass beaker with two-parallel CP (1.0 × 1.0 cm²) electrodes immersed in the acetone-catalyst suspension 1.0 cm apart. Then, +10 V bias was applied across the two electrodes for a predefined deposition time using a potentiostat (model VSP, BioLogic, Göttingen, Germany) and the electrocatalyst particles were coated on the negative electrode (cathode). After deposition, the working electrode was washed with distilled water and dried in an oven at 80 °C K for 2.0 h under an open atmosphere. The average weight of all mesoporous catalysts deposited on CP was approximately 0.8 mg.

Chronoamperometry and chronopotentiometry measurements were conducted to evaluate the durability of the fabricated electrode materials by fixing the current density or potentials. Electrochemical Impedance Spectroscopy (EIS) analysis was performed in the frequency range of 10^{-2} to 200 kHz with a 20-mV amplitude at a bias of 1.5 V vs. RHE in 1.0 M NaOH. The electrolyte solutions were deaerated with purged nitrogen gas for 15 min before the electrochemical measurements and the electrochemical experiments were repeated independently at least three times for each catalyst.

4. Conclusions

In summary, the effect of halide anions (F^{-} , Cl^{-} , and Br^{-}) doping on the structure and the induced electrochemical activity of the Sr_2CoO_4 perovskite catalyst has been systematically and comparatively examined using a range of characterization techniques. The physicochemical characterization results revealed that the halide anions doping, in particular the fluoride ion, enhanced the density of the surface oxygen vacancy defects, presumably due to weakening of the Co-O bonding and the withdraw of the electron density away from the Co-atom by halide ions. The comparative electrochemical activity performance of the oxyhalide-doped (F^{-} , Cl^{-} , and Br^{-}) catalysts revealed that the oxygen evolution reaction (OER) in alkaline was significantly improved, and the fluoride-doped exhibits the most superior activity among the investigated catalysts under static and steady-state conditions. The OE onset potential as well as the potential at current density of 10 mA/cm^2 were shifted to a lower values in the order of Sr_2CoO_4 (1.64, 1.73) > Sr_2CoO_3Br (1.61, 1.65) > Sr_2CoO_3Cl (1.53, 1.60) > Sr_2CoO_3F (1.50, 1.56) V vs. HRE. Moreover, Sr_2CoO_3F demonstrates remarkably less charge transfer resistance ($R_{ct} = 36.8 \text{ ohm}$) and long-term stability than the other oxyhalide counterparts during the OER. The doping of the perovskites with halide ions, particularly the fluoride-ion, enriches the oxygen vacancy defects due to electrons pulling away from the B-site of Co-atom that enhance the ionic and electronic conductivity as well as the electrochemical activity of the oxygen evolution reaction in alkaline solution. Generally, the strategy of halide anions doping at O-sites is an effective route to improve the electrochemical performance of perovskite-based oxides for oxygen evolution reaction.

Supplementary Materials: The following are available online at <https://www.mdpi.com/article/10.3390/catal11111408/s1>, Figure S1: Comparative XPS survey spectra of Sr_2CoO_4 , Sr_2CoO_3Br , Sr_2CoO_3Cl , and Sr_2CoO_3F catalysts, Fig. S2 linear sweep voltammetry (LSV) of Sr_2CoO_4 , Sr_2CoO_3Br , Sr_2CoO_3Cl , and Sr_2CoO_3F electrodes at rotation speed of 1600 rpm, in N_2 deaerated 1.0 M NaOH at a scan rate of 10 mV s^{-1} and catalyst loading of 0.8 mg/cm^2 , Table S1: Electrochemical activity comparison of strontium cobalt oxyhalides catalysts activities of OER onset overpotential and the overpotential required to achieve 10 mA/cm^2 current density ($\eta_{10 \text{ mA/cm}^2}$) with the benchmarking catalysts that reported in the literature.

Author Contributions: M.A.G. proposed the conceptualization plan, wrote the results and discussion, and submit the final manuscript; M.S.A. performed the experimental structure and electrochemical characterization and wrote the original draft; A.M.A.-M. supervise the whole project and revise the manuscript; P.A. carried out the data analysis and wrote the manuscript; M.T.W. prepared the catalysts, analyze and wrote the crystal structure. All authors have read and agreed to the published version of the manuscript.

Funding: This research was funded by the National Plan for Science, Technology, and Innovation (MAARIFAH), King Abdulaziz City for Science and Technology, Kingdom of Saudi Arabia, Award Number, Award Number **13-ENE-1227-02**.

Acknowledgments: This project was funded by the National Plan for Science, Technology, and Innovation (MAARIFAH), King Abdulaziz City for Science and Technology, Kingdom of Saudi Arabia, Award Number, Award Number **13-ENE-1227-02**.

Conflicts of Interest: The authors declare no conflict of interest.

References

1. Xia, W.; Mahmood, A.; Liang, Z.; Zou, R.; Guo, S. Earth-Abundant Nanomaterials for Oxygen Reduction. *Angew. Chemie-Int. Ed.* **2016**, *55*, 2650–2676. [[CrossRef](#)]
2. Wang, Z.L.; Xu, D.; Xu, J.J.; Zhang, X.B. Oxygen Electrocatalysts in Metal-Air Batteries: From Aqueous to Nonaqueous Electrolytes. *Chem. Soc. Rev.* **2014**, *43*, 7746–7786. [[CrossRef](#)]
3. Burke, M.S.; Enman, L.J.; Batchellor, A.S.; Zou, S.; Boettcher, S.W. Oxygen Evolution Reaction Electrocatalysis on Transition Metal Oxides and (Oxy)Hydroxides: Activity Trends and Design Principles. *Chem. Mater.* **2015**, *27*, 7549–7558. [[CrossRef](#)]
4. Tahir, M.; Pan, L.; Idrees, F.; Zhang, X.; Wang, L.; Zou, J.J.; Wang, Z.L. Electrocatalytic Oxygen Evolution Reaction for Energy Conversion and Storage: A Comprehensive Review. *Nano Energy* **2017**, *37*, 136–157. [[CrossRef](#)]
5. Walter, M.G.; Warren, E.L.; McKone, J.R.; Boettcher, S.W.; Mi, Q.; Santori, E.A.; Lewis, N.S. Solar Water Splitting Cells. *Chem. Rev.* **2010**, *110*, 6446–6473. [[CrossRef](#)]
6. Cook, T.R.; Dogutan, D.K.; Reece, S.Y.; Surendranath, Y.; Teets, T.S.; Nocera, D.G. Solar Energy Supply and Storage for the Legacy and Nonlegacy Worlds. *Chem. Rev.* **2010**, *110*, 6474–6502. [[CrossRef](#)] [[PubMed](#)]
7. Huang, Z.F.; Wang, J.; Peng, Y.; Jung, C.Y.; Fisher, A.; Wang, X. Design of Efficient Bifunctional Oxygen Reduction/Evolution Electrocatalyst: Recent Advances and Perspectives. *Adv. Energy Mater.* **2017**, *7*, 1–21. [[CrossRef](#)]
8. Yan, Y.; Xia, B.Y.; Zhao, B.; Wang, X. A Review on Noble-Metal-Free Bifunctional Heterogeneous Catalysts for Overall Electrochemical Water Splitting. *J. Mater. Chem. A* **2016**, *4*, 17587–17603. [[CrossRef](#)]
9. Jiao, Y.; Zheng, Y.; Jaroniec, M.; Qiao, S.Z. Design of Electrocatalysts for Oxygen-and Hydrogen-Involving Energy Conversion Reactions. *Chem. Soc. Rev.* **2015**, *44*, 2060–2086. [[CrossRef](#)]
10. Suntivich, J.; May, K.J.; Gasteiger, H.A.; Goodenough, J.B.; Shao-Horn, Y. A Perovskite Oxide Optimized for Oxygen Evolution Catalysis from Molecular Orbital Principles. *Science* **2011**, *334*, 1383–1385. [[CrossRef](#)] [[PubMed](#)]
11. Yang, W.; Salim, J.; Li, S.; Sun, C.; Chen, L.; Goodenough, J.B.; Kim, Y. Perovskite $\text{Sr}_{0.95}\text{Ce}_{0.05}\text{CoO}_{3-\delta}$ Loaded with Copper Nanoparticles as a Bifunctional Catalyst for Lithium-Air Batteries. *J. Mater. Chem.* **2012**, *22*, 18902–18907. [[CrossRef](#)]
12. Suntivich, J.; Gasteiger, H.A.; Yabuuchi, N.; Nakanishi, H.; Goodenough, J.B.; Shao-Horn, Y. Design Principles for Oxygen-Reduction Activity on Perovskite Oxide Catalysts for Fuel Cells and Metal-Air Batteries. *Nat. Chem.* **2011**, *3*, 546–550. [[CrossRef](#)] [[PubMed](#)]
13. Tanaka, H.; Misono, M. Advances in Designing Perovskite Catalysts. *Curr. Opin. Solid State Mater. Sci.* **2001**, *5*, 381–387. [[CrossRef](#)]
14. Harris, J. Low-Cost Oxygen Electrode Material. *Nature* **1970**, *226*, 848–849. [[CrossRef](#)]
15. Sunarso, J.; Torriero, A.A.J.; Zhou, W.; Howlett, P.C.; Forsyth, M. Oxygen Reduction Reaction Activity of La-Based Perovskite Oxides in Alkaline Medium: A Thin-Film Rotating Ring-Disk Electrode Study. *J. Phys. Chem. C* **2012**, *116*, 5827–5834. [[CrossRef](#)]
16. Hyodo, T.; Hayashi, M.; Miura, N.; Yamazoe, N. Catalytic Activities of Rare-Earth Manganites for Cathodic Reduction of Oxygen in Alkaline Solution. *J. Electrochem. Soc.* **1996**, *143*, L266–L267. [[CrossRef](#)]
17. Poux, T.; Napolskiy, F.S.; Dintzer, T.; Kéranguéven, G.; Istomin, S.Y.; Tsirlina, G.A.; Antipov, E.V.; Savinova, E.R. Dual Role of Carbon in the Catalytic Layers of Perovskite/Carbon Composites for the Electrocatalytic Oxygen Reduction Reaction. *Catal. Today* **2012**, *189*, 83–92. [[CrossRef](#)]
18. Malkhandi, S.; Trinh, P.; Manohar, A.K.; Manivannan, A.; Balasubramanian, M.; Prakash, G.K.S.; Narayanan, S.R. Design Insights for Tuning the Electrocatalytic Activity of Perovskite Oxides for the Oxygen Evolution Reaction. *J. Phys. Chem. C* **2015**, *119*, 8004–8013. [[CrossRef](#)]
19. Lee, D.U.; Park, H.W.; Park, M.G.; Ismayilov, V.; Chen, Z. Synergistic Bifunctional Catalyst Design Based on Perovskite Oxide Nanoparticles and Intertwined Carbon Nanotubes for Rechargeable Zinc-Air Battery Applications. *ACS Appl. Mater. Interfaces* **2015**, *7*, 902–910. [[CrossRef](#)]
20. Hardin, W.G.; Slanac, D.A.; Wang, X.; Dai, S.; Johnston, K.P.; Stevenson, K.J. Highly Active, Nonprecious Metal Perovskite Electrocatalysts for Bifunctional Metal-Air Battery Electrodes. *J. Phys. Chem. Lett.* **2013**, *4*, 1254–1259. [[CrossRef](#)]
21. Petrie, J.R.; Cooper, V.R.; Freeland, J.W.; Meyer, T.L.; Zhang, Z.; Lutterman, D.A.; Lee, H.N. Enhanced Bifunctional Oxygen Catalysis in Strained LaNiO_3 Perovskites. *J. Am. Chem. Soc.* **2016**, *138*, 2488–2491. [[CrossRef](#)] [[PubMed](#)]
22. Chang, H.; Bjørgum, E.; Mihai, O.; Yang, J.; Lein, H.L.; Grande, T.; Raaen, S.; Zhu, Y.-A.; Holmen, A.; Chen, D. Effects of Oxygen Mobility in La-Fe-Based Perovskites on the Catalytic Activity and Selectivity of Methane Oxidation. *ACS Catal.* **2020**, *10*, 3707–3719. [[CrossRef](#)]
23. Yang, W.; Hong, T.; Li, S.; Ma, Z.; Sun, C.; Xia, C.; Chen, L. Perovskite $\text{Sr}_{1-x}\text{Ce}_x\text{CoO}_{3-\delta}$ ($0.05 \leq x \leq 0.15$) as Superior Cathodes for Intermediate Temperature Solid Oxide Fuel Cells. *ACS Appl. Mater. Interfaces* **2013**, *5*, 1143–1148. [[CrossRef](#)]
24. Pan, X.; Wang, Z.; He, B.; Wang, S.; Wu, X.; Xia, C. Effect of Co Doping on the Electrochemical Properties of $\text{Sr}_2\text{Fe}_{1.5}\text{Mo}_{0.5}\text{O}_6$ Electrode for Solid Oxide Fuel Cell. *Int. J. Hydrog. Energy* **2013**, *38*, 4108–4115. [[CrossRef](#)]
25. Dai, N.; Feng, J.; Wang, Z.; Jiang, T.; Sun, W.; Qiao, J.; Sun, K. Synthesis and Characterization of B-Site Ni-Doped Perovskites $\text{Sr}_2\text{Fe}_{1.5-x}\text{Ni}_x\text{Mo}_{0.5}\text{O}_{6-\delta}$ ($x = 0, 0.05, 0.1, 0.2, 0.4$) as Cathodes for SOFCs. *J. Mater. Chem. A* **2013**, *1*, 14147–14153. [[CrossRef](#)]
26. Dai, H.X.; Ng, C.F.; Au, C.T. Perovskite-Type Halo-Oxide $\text{La}_{1-x}\text{Sr}_x\text{FeO}_{3-\Delta x \sigma}$ ($X = \text{F}, \text{Cl}$) Catalysts Selective for the Oxidation of Ethane to Ethene. *J. Catal.* **2000**, *189*, 52–62. [[CrossRef](#)]
27. Wang, Y.; Wang, H.; Liu, T.; Chen, F.; Xia, C. Improving the Chemical Stability of $\text{BaCe}_{0.8}\text{Sm}_{0.2}\text{O}_{3-\delta}$ Electrolyte by Cl Doping for Proton-Conducting Solid Oxide Fuel Cell. *Electrochem. Commun.* **2013**, *28*, 87–90. [[CrossRef](#)]

28. Yajima, T.; Takeiri, F.; Aidzu, K.; Akamatsu, H.; Fujita, K.; Yoshimune, W.; Ohkura, M.; Lei, S.; Gopalan, V.; Tanaka, K.; et al. A Labile Hydride Strategy for the Synthesis of Heavily Nitridized BaTiO. *Nat. Chem.* **2015**, *7*, 1017–1023. [[CrossRef](#)] [[PubMed](#)]
29. Li, Y.; Li, Y.; Wan, Y.; Xie, Y.; Zhu, J.; Pan, H.; Zheng, X.; Xia, C. Perovskite Oxyfluoride Electrode Enabling Direct Electrolyzing Carbon Dioxide with Excellent Electrochemical Performances. *Adv. Energy Mater.* **2019**, *9*, 1–10. [[CrossRef](#)]
30. Liu, Y.; Wang, W.; Xu, X.; Marcel Veder, J.P.; Shao, Z. Recent Advances in Anion-Doped Metal Oxides for Catalytic Applications. *J. Mater. Chem. A* **2019**, *7*, 7280–7300. [[CrossRef](#)]
31. Li, F.F.; Liu, D.R.; Gao, G.M.; Xue, B.; Jiang, Y.S. Improved Visible-Light Photocatalytic Activity of NaTaO₃ with Perovskite-like Structure via Sulfur Anion Doping. *Appl. Catal. B Environ.* **2015**, *166–167*, 104–111. [[CrossRef](#)]
32. Ruddlesden, S.N.; Popper, P. New Compounds of the K₂NiF₄ Type. *Acta Crystallogr.* **1957**, *10*, 538–539. [[CrossRef](#)]
33. Popper, S.R.P. Mixed Bismuth Oxides with Layer Lattices I. The Structure Type of CaNb₂Bi₂O. *Acta Crystallogr.* **1957**, *10*, 538.
34. Uma, S.; Raju, A.R.; Gopalakrishnan, J. Bridging the Ruddlesden-Popper and the Dion-Jacobson Series of Layered Perovskites: Synthesis of Layered Oxides, A_{2-x}La₂Ti_{3-x}Nb_xO₁₀ (A = K, Rb), Exhibiting Ion Exchange. *J. Mater. Chem.* **1993**, *3*, 709–713. [[CrossRef](#)]
35. Francis S., G. *Structure, Properties and Preparation of Perovskite-Type Compounds*; International Series of Monographs in Solid State Physics; Pergamon Press Ltd.: London, UK, 1969.
36. Takeguchi, T.; Yamanaka, T.; Takahashi, H.; Watanabe, H.; Kuroki, T.; Nakanishi, H.; Orihara, Y.; Uchimoto, Y.; Takano, H.; Ohguri, N.; et al. Layered Perovskite Oxide: A Reversible Air Electrode for Oxygen Evolution/Reduction in Rechargeable Metal-Air Batteries. *J. Am. Chem. Soc.* **2013**, *135*, 11125–11130. [[CrossRef](#)] [[PubMed](#)]
37. Grimaud, A.; May, K.J.; Carlton, C.E.; Lee, Y.L.; Risch, M.; Hong, W.T.; Zhou, J.; Shao-Horn, Y. Double Perovskites as a Family of Highly Active Catalysts for Oxygen Evolution in Alkaline Solution. *Nat. Commun.* **2013**, *4*, 1–7. [[CrossRef](#)] [[PubMed](#)]
38. Ghanem, M.A.; Arunachalam, P.; Almayouf, A.; Weller, M.T. Efficient Bi-Functional Electrocatalysts of Strontium Iron Oxy-Halides for Oxygen Evolution and Reduction Reactions in Alkaline Media. *J. Electrochem. Soc.* **2016**, *163*, H450–H458. [[CrossRef](#)]
39. Miyahara, Y.; Miyazaki, K.; Fukutsuka, T.; Abe, T. Strontium Cobalt Oxychlorides: Enhanced Electrocatalysts for Oxygen Reduction and Evolution Reactions. *Chem. Commun.* **2017**, *53*, 2713–2716. [[CrossRef](#)]
40. Tsujimoto, Y.; Sathish, C.I.; Matsushita, Y.; Yamaura, K.; Uchikoshi, T. New Members of Layered Oxychloride Perovskites with Square Planar Coordination: Sr₂MO₂Cl₂ (M = Mn, Ni) and Ba₂PdO₂Cl. *Chem. Commun.* **2014**, *50*, 5915–5918. [[CrossRef](#)] [[PubMed](#)]
41. Knee, C.; Price, D.; Lees, M.; Weller, M. Two-And Three-Dimensional Magnetic Order in the Layered Cobalt Oxychloride Sr₂CoO₃Cl. *Phys. Rev. B Condens. Matter Mater. Phys.* **2003**, *68*, 1–8. [[CrossRef](#)]
42. Tsujimoto, Y.; Yamaura, K.; Takayama-Muromachi, E. Oxyfluoride Chemistry of Layered Perovskite Compounds. *Appl. Sci.* **2012**, *2*, 206–219. [[CrossRef](#)]
43. Wang, X.L.; Takayama-Muromachi, E. Magnetic and Transport Properties of the Layered Perovskite System Sr_{2-y}Y_yCoO₄ (0 ≤ y ≤ 1). *Phys. Rev. B Condens. Matter Mater. Phys.* **2005**, *72*, 1–7.
44. Hector, A.L.; Knee, C.S.; MacDonald, A.I.; Price, D.J.; Weller, M.T. An unusual magnetic structure in Sr₂FeO₃F and magnetic structures of K₂NiF₄-type iron(III) oxides and oxide halides, including the cobalt substituted series Sr₂Fe_{1-x}Co_xO₃Cl. *J. Mater. Chem.* **2005**, *15*, 3093–3103. [[CrossRef](#)]
45. Knee, C.S.; Price, D.J.; Lees, M.R.; Weller, M.T. Two- and three-dimensional magnetic order in the layered cobalt oxychloride Sr₂CoO₃Cl. *Phys. Rev. B Condens. Matter Mater. Phys.* **2003**, *68*, 174407–174415. [[CrossRef](#)]
46. Akkerman, Q.A.; Manna, L. What Defines a Halide Perovskite? *ACS Energy Lett.* **2020**, *5*, 604–610. [[CrossRef](#)]
47. Dupin, J.-C.; Gonbeau, D.; Vinatier, P.; Levasseur, A. Systematic XPS studies of metal oxides, hydroxides and peroxides. *Phys. Chem. Chem. Phys.* **2000**, *2*, 1319. [[CrossRef](#)]
48. Lemoine, K.; Lhoste, J.; Hémon-Ribaud, A.; Heidary, N.; Maisonneuve, V.; Guiet, A.; Kornienko, N. Investigation of mixed-Metal (oxy)fluorides as a new class of water oxidation electrocatalysts. *Chem. Sci.* **2019**, *10*, 9209–9218. [[CrossRef](#)] [[PubMed](#)]
49. Zhang, L.; Sun, W.; Xu, C.; Ren, R.; Yang, X.; Qiao, J.; Wang, Z.; Sun, K. Attenuating a metal–Oxygen bond of a double perovskite oxide via anion doping to enhance its catalytic activity for the oxygen reduction reaction, *J. Mater. Chem. A* **2020**, *8*, 14091–14098. [[CrossRef](#)]